International Journal of Mechanical Sciences 52 (2010) 1491–1504

Contents lists available at ScienceDirect

International Journal of Mechanical Sciences

journal homepage: www.elsevier.com/locate/ijmecsci

A nonlinear analytical model for the squeeze-film dynamics of parallel plates subjected to axial flow

José Antunes [a], Philippe Piteau [b,*]

[a] Instituto Tecnológico e Nuclear, Applied Dynamics Laboratory, ITN/ADL, 2686 Sacavem codex, Portugal
[b] Commissariat à l'Energie Atomique, Laboratoire d'Études de Dynamique, CEA-Saclay/DEN/DM2S/SEMT/DYN, 91191 Gif-sur-Yvette Cedex, France

ARTICLE INFO

Article history:
Received 5 February 2010
Received in revised form
6 May 2010
Accepted 23 May 2010
Available online 27 May 2010

Keywords:
Flow-structure interaction
Flow-induced vibrations
Nonlinear dynamics
Squeeze-film dynamics

ABSTRACT

In this paper, we develop a theoretical model to predict the nonlinear fluid–structure interaction forces and the dynamics of parallel vibrating plates subjected to an axial gap flow. The gap is assumed small, when compared to the plate dimensions, the plate width being much larger than the length, so that the simplifying assumptions of 1D bulk-flow models are adequate. We thus develop a simplified theoretical squeeze-film formulation, which includes both the distributed and singular dissipative flow terms. This model is suitable for performing effective time-domain numerical simulations of vibrating systems which are coupled by the nonlinear unsteady flow forces, for instance the vibro-impact dynamics of plates with fluid gap interfaces. A linearized version of the flow model is also presented and discussed, which is appropriate for studying the complex modes and linear stability of flow/structure coupled systems as a function of the average axial gap velocity. Two applications of our formulation are presented: (1) first we study how an axial flow modifies the rigid-body motion of immersed plates falling under gravity; (2) then we compute the dynamical behavior of an immersed oscillating plate as a function of the axial gap flow velocity. Linear stability plots of oscillating plates are shown, as a function of the average fluid gap and of the axial flow velocity, for various scenarios of the loss terms. These results highlight the conditions leading to either the divergence or flutter instabilities. Numerical simulations of the nonlinear flow/structure dynamical responses are also presented, for both stable and unstable regimes. This work is of interest to a large body of real-life problems, for instance the dynamics of nuclear spent fuel racks immersed in a pool when subjected to seismic excitations, or the self-excited vibro-impact motions of valve-like components under axial flows.

1. Introduction

Many systems of practical interest are subjected to intense fluid/structure interaction forces when a thin layer of fluid is interposed between two vibrating structures. A typical example is provided by immersed structural components, which may impact if an external excitation is imposed. Nonlinear effects can then become dominant and should not be neglected. Significant work in this field has been performed at CEA/Saclay during the last two decades, in connection with nuclear facilities (see [1,2]). However, to our best knowledge, all previous nonlinear studies were limited to systems which vibrate and impact under no-flow conditions. This constitutes a severe limitation which may lead to erroneous predictions of the interaction forces and of the system motions. In particular, self-excited motion regimes may arise, which obviously cannot be predicted using a "stagnant" flow formulation.

On the other hand, the extensive literature on the fluid/structure dynamics of industrial squeeze-film problems is mostly concerned with linearized analysis, when the vibratory motions are such that, at each location $\mathbf{r}$, the fluctuating part $\tilde{h}(\mathbf{r},t)$ of the local fluid gap $h(\mathbf{r},t)=\overline{h}(\mathbf{r})+\tilde{h}(\mathbf{r},t)$ is small compared to the mean gap value $\overline{h}(\mathbf{r})$ (see, for instance, works by Fritz [3], Hobson [4], Mulcahy [5,6], Inada and Hayama [7,8], Perotin and Granger [9], Porcher and DeLangre [10], Inada and Hayama [11], Kaneko et al. [12] or Moreira et al. [13], as well as the review books by Païdoussis [14] and Kaneko et al. [15]). One of the most thorough analysis along these lines was achieved by Inada and Hayama [7], who evaluated the fluidelastic force under steady flow, including added mass, damping and stiffness flow terms for an one-dimensional tapered leakage channel. More recently, Porcher and DeLangre [10] evaluated the dynamical effects of changing the loss coefficients at the channel inlet and outlet boundary conditions.

The linearized approach is adequate for stability studies, which are often the primary concern, but obviously unable to provide answers at larger vibratory amplitudes, when the fluctuating gap $\tilde{h}(\mathbf{r},t)$ is of the same order of magnitude as $\overline{h}(\mathbf{r})$. Such is the case, in

* Corresponding author.
E-mail addresses: jantunes@itn.pt (J. Antunes), philippe.piteau@cea.fr (P. Piteau).

0020-7403/$ - see front matter © 2010 Elsevier Ltd. All rights reserved.
doi:10.1016/j.ijmecsci.2010.05.009

Nomenclature

C_s	structural damping
$C_1(t)$, $C_2(t)$	integration "constants" for the dynamical pressure field
$F_e(t)$	external force
$\overline{F}_e$	mean value of the external force
$\tilde{F}_e(t)$	fluctuating component of the external force
$F_f(t)$	fluid/structure coupling force per unit width of the plate
$\overline{F}_f$	mean value of the fluid coupling force
$\tilde{F}_f(t)$	fluctuating component of the fluid coupling force
$\hat{F}_f$	complex amplitude of the oscillatory fluid force
$f_1 f_2$	friction coefficients for the distributed tangential flow stresses
f_s	structural in vacuum plate frequency
H	fluid gap under static and no-flow conditions
$h(\mathbf{r},t)$	fluid gap
$\overline{h}(\mathbf{r})$	mean value of the fluid gap
$\tilde{h}(\mathbf{r},t)$	fluctuating component of the fluid gap
K_{In}	singular loss coefficient for the entering flow at the plate boundaries
K_{Out}	singular loss coefficient for the exiting flow at the plate boundaries
K_s	structural stiffness
$L \equiv L_x$	lower dimension of the plate (length)
$L_x \times L_z$	plate dimensions (length × width)
M_a	fluid added mass
M_s	structural mass
m,n	coefficients of Hirs' correlation for the friction coefficient
P_A, P_B	external static pressures at the left-side ($x=0^-$) and right-side ($x=L^+$) fluid reservoirs
P_{ext}	identical external static pressures at the left-side and right-side fluid reservoirs (symmetrical case)
$P(x,y,z,t)$	flow pressure 3D field
$P(\mathbf{r},t)$	bulk-flow pressure field
$\mathbf{r} \equiv \{x,z\}$	location along the system
Re	Reynolds number of the flow
t	time
$\mathcal{T}$	dimensionless time
$U(t) \equiv C_1(t)$	space-independent unsteady component of the axial flow velocity
$\overline{U}$	mean value of the axial flow velocity
$\overline{\mathcal{U}}$	dimensionless mean value of the axial flow velocity
$\tilde{U}(t)$	fluctuating component of the axial flow velocity
$\tilde{\mathcal{U}}(t)$	dimensionless fluctuating component of the axial flow velocity
$\hat{U}$	complex amplitude of the oscillatory axial flow velocity
$u(\mathbf{r},t)$	bulk-flow velocity field (x component)
$v(\mathbf{r},t)$	bulk-flow velocity field (z component)
$V_x(x,y,z,t)$	flow velocity 3D field (x component)
$V_z(x,y,z,t)$	flow velocity 3D field (z component)
$X_1 \equiv Y$	plate displacement in state-space formulation
$\tilde{\mathcal{X}}_1 \equiv \tilde{\mathcal{Y}}$	dimensionless plate displacement in state-space formulation
$X_2 \equiv \dot{Y}$	plate velocity in state-space formulation
$\tilde{\mathcal{X}}_2 \equiv \dot{\tilde{\mathcal{Y}}}$	dimensionless plate velocity in state-space formulation
x	coordinate along the direction of dimension L_x
$Y(t)$	vertical motion of the upper plate
$\overline{Y}$	mean value of the plate displacement
$\tilde{Y}(t)$	fluctuating component of the plate displacement
$\tilde{\mathcal{Y}}(t)$	dimensionless fluctuating component of the plate displacement
$\hat{Y}$	complex amplitude of the oscillatory plate displacement
z	coordinate along the direction of dimension L_z
$\Delta P = P_A - P_B$	difference between the left side and right-side reservoir static pressures
ε	reduced gap parameter
$\lambda_n = \sigma_n \pm i\omega_n$	complex eigenvalues of the linearized problem
η	reduced mass parameter
ν	fluid kinematic viscosity
ω	motion frequency
ω_0	modal frequency of the plate in still fluid
ω_n	imaginary part of the complex eigenvalues of the linearized problem (damped modal frequency)
ρ	fluid volumic mass
σ_n	real part of the complex eigenvalues of the linearized problem
τ_1^x, τ_1^z	shear stresses at the fluid/wall interface of plate 1
τ_2^x, τ_2^z	shear stresses at the fluid/wall interface of plate 2
ζ_s	structural in vacuum plate damping
ζ_0	modal damping of the plate in still fluid
$\zeta_n = -\sigma_n/\lvert\lambda_n\rvert$	modal damping of the linearized problem

particular, beyond the stability boundaries, when addressing the nonlinear responses of self-excited systems. Finding a suitable analytical formulation for the fully nonlinear problem is the main subject of the present paper, where we extend previous efforts in this field, in order to cope with the nonlinear coupling terms which arise when the fluid between the vibrating surfaces is subjected to axial flow.

Overall, the analytical formulation developed here may be connected with our approach in work focused on immersed rotor dynamics (see [13,16–20]). Indeed, the successful "bulk-flow" approach started by Fritz [3] and Hirs [21], and later used by many authors (see [22]) appears also well suited to deal with the small-to-moderate fluctuating gaps, such as found in the configuration of the present problem. We will start by deriving a nonlinear flow model under no-flow conditions. Apart from the specific dissipative terms connected with our quadratic-in-velocity pressure-drop formulation, we obtain fluid forces which are similar to those previously presented by Esmonde et al. [1]. Then we extend our formulation to the interesting case of vibrating surfaces subjected to an axial flow. The nonlinear model is then linearized, and a considerably simpler formulation is obtained which is convenient when $\tilde{h}/\overline{h} \ll 1$.

As noted by a several authors [10,13,18,20], dissipative terms induce frequency-dependent delay effects for systems subjected to steady flows. Here, similarly to the approach originally developed by Moreira et al. [13,20], the frequency-dependent terms are conveniently integrated by using an additional variable (related to the fluctuating axial flow-rate), and dynamically formulated through a first-order nonlinear differential equation. This approach enabled us to completely avoid iterations while evaluating the nonlinear dynamics of coupled systems, or when computing eigenvalues of the corresponding linearized problems.

To complete the paper we present numerical simulations of systems which present both practical and academic interest. Our first example concerns the motion of a gravity-driven plate colliding with a rigid plane surface, as a function of the axial flow velocity. This example is motivated by impact problems which may arise between immersed nuclear components, such as fuel

racks. We also present examples of vibrating structures under axial flows, which are illustrated by eigenvalue computations and nonlinear simulations. Depending on the flow and on the structural parameters, various dynamical regimes are obtained, in particular nonlinear post-stable limit-cycles. Hence, the present model may be useful for many dynamical predictions, ranging from vibro-impact problems in industrial components to musical instruments. Limited experimental results are available at the present time (see [23]), which should be extended in future work.

2. Nonlinear theory

2.1. Flow equations

To derive the bulk-flow equations for the flow within a small-to-moderate fluctuating gap, the control volume shown in Fig. 1 applies, where the gap $h(\mathbf{r},t)$ between the vibrating plates 1 and 2 is filled with an incompressible fluid of volumic mass ρ.

As mentioned before, at each location $\mathbf{r}\equiv\{x,z\}$ we define $h(\mathbf{r},t)=\bar{h}(\mathbf{r})+\tilde{h}(\mathbf{r},t)$, where $\bar{h}(\mathbf{r})$ is the average value of the local gap between the non-vibrating plates under steady flow and load conditions. Because the transverse gap $h(\mathbf{r},t)$ is assumed small with respect to the longitudinal plate dimensions L_x (length) and L_z (width), in the bulk-flow modeling approach one neglects the changes in pressure and velocity across the fluid gap, so that we may conveniently replace the pressure field $P(x,y,z,t)$ and the components $V_x(x,y,z,t)$ and $V_z(x,y,z,t)$ of the velocity field by their gap-averaged values:

$$p(\mathbf{r},t)\equiv p(x,z,t)=\int_0^{h(x,z,t)} P(x,y,z,t)\,dy \tag{1}$$

$$u(\mathbf{r},t)\equiv u(x,z,t)=\int_0^{h(x,z,t)} V_x(x,y,z,t)\,dy,\quad v(\mathbf{r},t)\equiv v(x,z,t)=\int_0^{h(x,z,t)} V_z(x,y,z,t)\,dy \tag{2}$$

Then, considering a small control volume CV across the fluid gap thickness, with whole boundary CS, the continuity equation is written as

$$\frac{\partial}{\partial t}\iiint_{CV}\rho\,dV+\iint_{CS}\rho\mathbf{V}\cdot\mathbf{n}\,dS=0 \tag{3}$$

where $\mathbf{V}$ is the velocity of the fluid crossing CS and $\mathbf{n}$ is the local unit vector normal to the boundary. The momentum equation is written as

$$\frac{\partial}{\partial t}\iiint_{CV}\mathbf{V}\rho\,dV+\iint_{CS}\mathbf{V}\rho\mathbf{V}\cdot\mathbf{n}\,dS=\sum_n\mathbf{F}_n \tag{4}$$

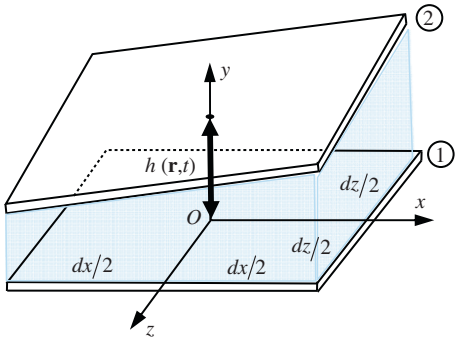

Fig. 1. Control volume used for deriving the bulk-flow equations.

where $\mathbf{F}_n$ are the external and volumic forces acting the fluid in CV. Referring to the elementary control volume shown in Fig. 1, one obtains (see, for instance, [6] or [1]):

$$\frac{\partial}{\partial t}\iiint_{CV}\rho\,dV=\frac{\partial}{\partial t}(\rho h)\,dx\,dz,\qquad \iint_{CS}\rho\mathbf{V}\cdot\mathbf{n}\,dS=\frac{\partial}{\partial x}(\rho hu)\,dx\,dz+\frac{\partial}{\partial z}(\rho hv)\,dx\,dz \tag{5}$$

so that the continuity equation reads:

$$\frac{\partial h}{\partial t}+\frac{\partial}{\partial x}(hu)+\frac{\partial}{\partial z}(hv)=0 \tag{6}$$

On the other hand, the component terms of the momentum equation are given as

$$\begin{aligned}\frac{\partial}{\partial t}\iiint_{CV}\mathbf{V}\rho\,dV&=\left[\frac{\partial}{\partial t}(\rho hu)\,dx\,dz\right]\mathbf{i}+\left[\frac{\partial}{\partial t}(\rho hv)\,dx\,dz\right]\mathbf{k}\\ \iint_{CS}\mathbf{V}\rho\mathbf{V}\cdot\mathbf{n}\,dS&=\left[\frac{\partial}{\partial x}(\rho hu^2)\,dx\,dz+\frac{\partial}{\partial z}(\rho huv)\,dx\,dz\right]\mathbf{i}\\ &\quad+\left[\frac{\partial}{\partial x}(\rho huv)\,dx\,dz+\frac{\partial}{\partial z}(\rho hv^2)\,dx\,dz\right]\mathbf{k}\\ \sum_n\mathbf{F}_n&=\left[\left(-\tau_1^x-\tau_2^x-h\frac{\partial p}{\partial x}\right)dx\,dz\right]\mathbf{i}+\left[\left(-\tau_1^z-\tau_2^z-h\frac{\partial p}{\partial z}\right)dx\,dz\right]\mathbf{k}\end{aligned} \tag{7}$$

where as discussed in Section 2.2, τ_1^x, τ_2^x, τ_1^z and τ_2^z are the shear stresses at the fluid/wall interfaces of plates 1 and 2, respectively, along the orthogonal directions of the unit vectors $\mathbf{i}$ and $\mathbf{k}$. Then, the momentum equation (4) leads to the following scalar equations:

$$\rho\left[\frac{\partial}{\partial t}(hu)+\frac{\partial}{\partial x}(hu^2)+\frac{\partial}{\partial z}(huv)\right]=-\left(\tau_1^x+\tau_2^x+h\frac{\partial p}{\partial x}\right) \tag{8}$$

$$\rho\left[\frac{\partial}{\partial t}(hv)+\frac{\partial}{\partial x}(huv)+\frac{\partial}{\partial z}(hv^2)\right]=-\left(\tau_1^z+\tau_2^z+h\frac{\partial p}{\partial z}\right) \tag{9}$$

For the geometry of interest here, shown in Fig. 2, we are interested in the flow between two plates such that $(L\equiv L_x)\ll L_y$, therefore, we may postulate $v\ll u$. Then, Eqs. (6), (8) and (9) reduce to the following 1D formulation:

$$\frac{\partial h}{\partial t}+\frac{\partial}{\partial x}(hu)=0 \tag{10}$$

and

$$\rho\left[\frac{\partial}{\partial t}(hu)+\frac{\partial}{\partial x}(hu^2)\right]=-\left(\tau_1^x+\tau_2^x+h\frac{\partial p}{\partial x}\right) \tag{11}$$

Furthermore, because the plate surfaces will in this paper be assumed parallel, we have $h(x,t)=Y(t)$, $\forall x$, where for simplicity it will be assumed that the lower plate is fixed and the fluid gap $Y(t)$ is given by the displacement of the upper plate. Finally,

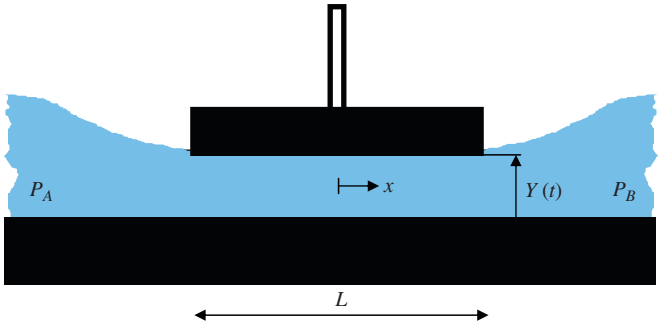

Fig. 2. Geometry of the flow-structure system.

Eqs. (10) and (11) become

$$\frac{\partial Y}{\partial t}+Y\frac{\partial u}{\partial x}=0 \tag{12}$$

$$\rho\left[\frac{\partial}{\partial t}(Yu)+Y\frac{\partial}{\partial x}(u^2)\right]+\tau_1^x+\tau_2^x+Y\frac{\partial p}{\partial x}=0 \tag{13}$$

and the dynamic force exerted by the fluid per unit width of the plate – e.g., the total force is $L_zF_f(t)$ – is given by

$$F_f(t)=\int_{-L/2}^{L/2}p(x,t)\,dx \tag{14}$$

2.2. Dissipative phenomena

Following the bulk-flow approach, the tangential stresses τ_1^x and τ_2^x will be formulated using a loss-of-head model:

$$\tau_{1,2}^x=\frac{1}{2}\rho u|u|f_{1,2} \tag{15}$$

where the friction coefficients at the walls f_1 and f_2 are established based on empirical correlations (see [24,25]). Typically, f changes with the flow Reynolds number as [21]

$$f=n(\mathrm{Re})^m=n\left(\frac{uh}{\nu}\right)^m \tag{16}$$

where parameters m and n depend on the flow. For turbulent flows between plane smooth surfaces, Hirs suggest the following values:

$$10^3<\mathrm{Re}<310^4\Rightarrow m=-0.25,\quad n=0.055\Rightarrow f=\frac{0.055}{\sqrt[4]{\mathrm{Re}}} \tag{17}$$

otherwise, the Blasius friction correlation can be used with almost similar results:

$$f=\frac{0.0665}{\sqrt[4]{\mathrm{Re}}} \tag{18}$$

On the other hand, for laminar flows, the friction coefficient decreases very fast for increasing flow velocities. In rectangular channel it can be easily shown that:

$$\mathrm{Re}<410^3\Rightarrow f=\frac{12}{\mathrm{Re}} \tag{19}$$

Beyond these distributed stresses, other singular dissipative effects arise in the boundaries $x=\pm L/2$ of the moving plate. Very complex phenomena arise here, which may be modeled in a simplified manner using a quasi-static Bernoulli formulation. We then obtain, for instance at $x=L/2$:

$$p\left(\frac{L}{2},t\right)+\frac{1}{2}\rho u\left(\frac{L}{2},t\right)^2=P_{ext}+\frac{1}{2}\rho u\left(\frac{L}{2},t\right)\left|u\left(\frac{L}{2},t\right)\right|K_{In,Out} \tag{20}$$

where P_{ext} is a static reference pressure in an external reservoir, far from the singularity, and the loss coefficients $K_{In,Out}$ depend on the local geometry and Reynolds number. For turbulent flows and an abrupt gap change, typical values are given by [25] $K_{In}\approx 0.5$ (when $\dot{Y}(t)>0$) and $K_{Out}\approx 1$ (when $\dot{Y}(t)<0$). In short, this means that about half the kinetic energy of the inflow and the full kinetic energy of the outflow is lost through irreversible phenomena. Idel'Cik [24] and Blevins [25] present detailed data for many boundary shapes. In general, smooth (rounded) corners of the plates at $x=\pm L/2$ will lead to lower values of K_{In}. On the other hand, low velocity flows will lead to increased values of the loss coefficient.

2.3. Solution without permanent axial flow

The dynamical response of parallel plates separated by a stagnant fluid constitutes the much simpler problem studied by Esmonde et al. [1]. Here, the external static pressure P_A on reservoir at the left side of the plate is equal to the static pressure P_B on the right side, $P_A=P_B\equiv P_{ext}$. We also postulate that the plate surfaces are similar, so that $f_1=f_2\equiv f$ and we obtain from Eqs. (12) and (13):

$$\frac{\partial u}{\partial x}=-\frac{\dot{Y}}{Y} \tag{21}$$

$$\frac{\partial p}{\partial x}=-\rho\left[\dot{u}+\frac{u\dot{Y}}{Y}+2u\frac{\partial u}{\partial x}+\frac{u|u|}{Y}f\right] \tag{22}$$

with $Y(t)>0$, $\forall t$. It appears immediately that, when $Y\to 0$, the flow-generated force will tend to infinity. Accounting for the problem symmetry, the direct integration of Eq. (21) provides the velocity field:

$$u(x,t)=-x\frac{\dot{Y}}{Y} \tag{23}$$

and from Eq. (22), applying the boundary conditions discussed in Section 2.2, the pressure field becomes:

$$p(x,t)=P_{ext}-\frac{1}{2}\rho\left[\left(\frac{L}{2}\right)^2-x^2\right]\frac{\ddot{Y}}{Y}+\rho\left[\frac{1}{2}\left(\frac{L}{2}\right)^2-x^2\right]\frac{\dot{Y}^2}{Y^2}-\frac{1}{3}\rho\left[\left(\frac{L}{2}\right)^3-x^3\right]\frac{\dot{Y}|\dot{Y}|}{Y^3}f-\frac{1}{8}\rho L^2\frac{\dot{Y}|\dot{Y}|}{Y^2}K_{In,Out} \tag{24}$$

Note that, in the previous integration, the friction coefficient f was assumed constant in space, which is in strictly not true. Indeed, from Eq. (16) it is seen that the friction coefficient depends on $u(x,t)$, so that one has in general $f(x,t)$. However, experimental evidence show that for turbulent flows the exponent m in Eq. (17) is quite small (in many cases almost zero), so that the change of the friction coefficient with flow velocity becomes second order. Hence, for turbulent flows, the preceding simplification is well justified. However, if the flow velocity is low enough, laminar flows will arise such that $f\sim O(1/u)$ (see Eq. (19)), and the convenient simplification adopted here will lead to some error. Notice that such is the case, in particular, for the geometry of Fig. 2 under no permanent axial flow. Indeed, symmetry imposes that near the middle of the plate $u(0,t)=0$, therefore a (smaller or larger) region of the channel will always display laminar flow. This difficulty will be addressed elsewhere, because in this paper we are mostly concerned about the vibrations of plates subjected to a permanent axial flow which is often turbulent, therefore the above-mentioned inadequacy will be tolerated.

From Eqs. (14) and (24), we obtain following explicit form for the total dynamic force of the fluid on the plates, per unit width:

$$F_f(t)=P_{ext}L-\frac{\rho L^3}{12}\frac{\ddot{Y}}{Y}+\frac{\rho L^3}{24}\frac{\dot{Y}^2}{Y^2}-\frac{\rho L^4}{32}\frac{\dot{Y}|\dot{Y}|}{Y^3}f-\frac{\rho L^3}{8}\frac{\dot{Y}|\dot{Y}|}{Y^2}K_{In,Out} \tag{25}$$

In solution (25) one can recognize, beyond the trivial constant force term stemming from P_{ext}, four vibration-induced nonlinear dynamical terms which are related to: (a) the local fluid inertia, (b) the convective inertia, (c) the distributed wall interface stresses, and (d) the singular losses at the boundaries. Notice that the magnitude of all these force terms increase dramatically as the fluid gap closes, because of the various powers of $Y(t)$ in the denominators of Eq. (25)—hence the squeeze-film effect.

Most terms in solution (25) are analogous to those published by Esmonde et al. [1]. However, our quadratic dissipative term related to flow/wall stresses is different from theirs, due to the distinct assumptions involved. Both coefficients K_{In} and K_{Out} can be used when performing a numerical simulation, the first one

during aspiration ($\dot{Y}(t)>0$) and the other during ejection ($\dot{Y}(t)<0$).

2.4. Solution with permanent axial flow

For a more general flow configuration, the problem symmetry is broken. We will now assume that the external static pressure P_A on the left side of the plate is higher than the static pressure P_B on the right side. A permanent flow is thus generated, directed from left to right, which increases with the ratio P_A/P_B. Integration of the continuity equation will now lead to the general velocity field:

$$u(x,t)=-x\frac{\dot{Y}}{Y}+C_1(t) \tag{26}$$

Then, from Eqs. (22) and (26) we get

$$\begin{aligned}p(x,t)=&\frac{1}{2}\rho x^2\frac{\ddot{Y}}{Y}-\rho x^2\frac{\dot{Y}^2}{Y^2}+\rho x\frac{\dot{Y}}{Y}C_1(t)\\&+\frac{1}{3}\rho\left[\left(x^2\frac{\dot{Y}}{Y^2}-2x\frac{C_1(t)}{Y}+C_1(t)^2\dot{Y}\right)\left|x\frac{\dot{Y}}{Y}-C_1(t)\right|\right.\\&\left.-C_1^2(t)|C_1(t)|\dot{Y}\right]f-\rho x\dot{C}_1(t)+C_2(t)\end{aligned} \tag{27}$$

and the integration "constants" $C_1(t)$ and $C_2(t)$ are computed by enforcing the boundary conditions:

$$p\left(-\frac{L}{2},t\right)=P_A-\frac{1}{2}\rho u\left(-\frac{L}{2},t\right)^2-\frac{1}{2}\rho u\left(-\frac{L}{2},t\right)\left|u\left(-\frac{L}{2},t\right)\right|\overline{K}_A \tag{28}$$

$$p\left(\frac{L}{2},t\right)=P_B-\frac{1}{2}\rho u\left(\frac{L}{2},t\right)^2+\frac{1}{2}\rho u\left(\frac{L}{2},t\right)\left|u\left(\frac{L}{2},t\right)\right|\overline{K}_B \tag{29}$$

where to simplify the formulation, $\overline{K}_A$ and $\overline{K}_B$ stand for the *average* values of the corresponding inflow and outflow loss coefficients.

The inflow and outflow singular loss coefficients are usually different and, furthermore, usually depend on the flow Reynolds number. Then, using "average" values for single inflow/outflow coefficients constitute a convenient but obviously rough approximation. For the nonlinear time-domain computations, nothing prevent us from using time-varying friction coefficients, function of the local time-varying Reynolds number. For the time-domain formulation, one can then take the "average" friction coefficients simply as a notational convenience. Notice, however, that the friction coefficients available in the literature were obtained for steady flows, and that their use under unsteady conditions – although a common practice – is a least debatable. Even so, because very few experimental data is available on unsteady friction coefficients, the use of steady coefficients adopted in this paper – in spite of entailing obvious pertinent criticisms – follows the most current practice. However, having accepted such crude approximation, it seems reasonable (even for the time-domain nonlinear computations) to use constant friction coefficients, with "average" values (in the sense of time-averaged) such that they fit reasonably well the actual range of Reynolds numbers of the computed motion. The values adopted must be based on estimates of the inflow and outflow Reynolds numbers, and may eventually be refined in an iterative manner, from the computated flow results, so that the "average" singular loss coefficients be as compatible as possible with the resulting inflows and outflows, for the computed range of Reynolds numbers. Clearly, this constitutes a less-than-satisfactory issue, but sometimes convenience prevails, when the better alternative is exceedingly involved or asks for nonexistent experimental data.

For vibrating plates subjected to symmetrical boundary conditions, there is no net axial flow, and therefore there is inflow when the plates separate and outflow when they approach. This simple geometrical fact enables an easy distinction of when one should apply inflow or outflow values for the singular loss coefficients. Then, for the nonlinear computations, it is reasonable to apply different values of the friction coefficients, according to the motion stage of the plate, which causes the flow to enter or exit the channel. However, when the pressure boundary conditions are non-symmetrical, there is a net axial flow which prevents the use of a simple relationship between the plate motions and the nature of the flow. The flow velocity direction in each point now depend on both the pressure-induced axial flow as well as on the plate motion $Y(t)$. Therefore, in contrast with the basic case discussed in Section 2.3, inflow and outflow are not simply related to conditions $\dot{Y}(t)>0$ or $\dot{Y}(t)<0$, as flow patterns can be much more complex and one cannot state, a priori, the nature of the flow from the plate motions. Under such conditions, it may be reasonable to use suitable "average" values for the loss coefficients, which should be representative as much as possible of the full inlet/outlet cycle. Also notice that, for linearized analysis of the flow-coupled system, one cannot use time-dependent friction coefficients. The ultimate compromise of using constant average loss coefficients representative of the full inlet/outlet cycle then becomes mandatory. If plate boundaries are abrupt, average loss values $0.5 < \overline{K}_{A,B} < 1$ should be used for turbulent flows, the upper boundary increasing somewhat for laminar flows (see [24]). These issues are investigated in greater detail by Piteau and Antunes [26].

Equating the left-side and right-side boundary conditions (28) and (29), we compute $C_1(t)$ and $C_2(t)$ in Eq. (27). Then, integration of the pressure field leads to the dynamic force per unit width

$$\begin{aligned}F_f(t)=&\frac{L}{2}(P_A+P_B)-\frac{\rho L^3}{12}\frac{\ddot{Y}}{Y}+\frac{\rho L^3}{24}\frac{\dot{Y}^2}{Y^2}-\frac{\rho L^2}{8}\frac{\dot{Y}}{Y}\left[\left(\frac{fL}{4Y}+\overline{K}_A\right)\left|\frac{L}{2}\frac{\dot{Y}}{Y}+C_1(t)\right|\right.\\&\left.+\left(\frac{fL}{4Y}+\overline{K}_B\right)\left|-\frac{L}{2}\frac{\dot{Y}}{Y}+C_1(t)\right|\right]+\frac{f\rho}{12}\frac{Y}{\dot{Y}^2}\left(\left|\frac{L}{2}\frac{\dot{Y}}{Y}+C_1(t)\right|\right.\\&\left.-\left|-\frac{L}{2}\frac{\dot{Y}}{Y}+C_1(t)\right|\right)C_1(t)^3-\frac{\rho L}{2}\left[\frac{f}{12\dot{Y}}\left(\left|\frac{L}{2}\frac{\dot{Y}}{Y}+C_1(t)\right|\right.\right.\\&\left.\left.+\left|-\frac{L}{2}\frac{\dot{Y}}{Y}+C_1(t)\right|\right)+1\right]C_1(t)^2-\frac{\rho L}{4}\left[\left(\frac{5fL}{12Y}+\overline{K}_A\right)\left|\frac{L}{2}\frac{\dot{Y}}{Y}+C_1(t)\right|\right.\\&\left.-\left(\frac{5fL}{12Y}+\overline{K}_B\right)\left|-\frac{L}{2}\frac{\dot{Y}}{Y}+C_1(t)\right|\right]C_1(t)\end{aligned} \tag{30}$$

where $C_1(t)$ is expressed in terms of the following nonlinear differential equation:

$$\begin{aligned}\dot{C}_1(t)=&\frac{1}{\rho L}(P_A-P_B)-\frac{f}{3L\dot{Y}}\left[\left|\frac{L}{2}\frac{\dot{Y}}{Y}+C_1(t)\right|-\left|-\frac{L}{2}\frac{\dot{Y}}{Y}+C_1(t)\right|\right]C_1(t)^2\\&-\left[\left(\frac{f}{3Y}+\frac{\overline{K}_A}{2L}\right)\left|\frac{L}{2}\frac{\dot{Y}}{Y}+C_1(t)\right|+\left(\frac{f}{3Y}+\frac{\overline{K}_B}{2L}\right)\left|-\frac{L}{2}\frac{\dot{Y}}{Y}+C_1(t)\right|\right]C_1(t)\\&-\frac{\dot{Y}}{Y}\left[\left(\frac{fL}{12Y}+\frac{\overline{K}_A}{4}\right)\left|\frac{L}{2}\frac{\dot{Y}}{Y}+C_1(t)\right|-\left(\frac{fL}{12Y}+\frac{\overline{K}_B}{4}\right)\left|-\frac{L}{2}\frac{\dot{Y}}{Y}+C_1(t)\right|\right]\end{aligned} \tag{31}$$

These flow-related equations are coupled with the structural dynamical equation for the plate dynamics, through:

$$M_s\ddot{Y}+C_s\dot{Y}+K_s[Y-H]=L_zF_f(t)+F_e(t) \tag{32}$$

where L_z is the plate width, H is the fluid gap under static conditions and no-flow, M_s, C_s and K_s are structural parameters, $F_f(t)$ is the flow coupling force previously discussed and $F_e(t)$ stands for any other external force, such as a shaker. Eqs. (30)–(32) must be solved simultaneously using any suitable time-step

integration technique, for the initial conditions $Y(0)=Y_0$, $\dot{Y}(0)=\dot{Y}_0$ and $C_1(0)=C_0$.

Derivation of solution (30) and (31) is rather tedious, and is greatly alleviated by using symbolic manipulators, such as Maple [27]. One may verify that this general solution reverts to the previous symmetrical no-flow problem, when $P_A=P_B=P_{ext}$ and $\overline{K}_A=\overline{K}_B=\overline{K}$, in which case $C_1(t)\equiv 0$. On the other hand, the physical meaning of $C_1(t)$ becomes clear from Eq. (26), where a motion-dependent space-symmetrical velocity term is superposed to $C_1(t)$. The space integral of the first term is null, so that

$$U(t)=\frac{1}{L}\int_{-L/2}^{L/2}u(x,t)\,dx=\frac{1}{L}\int_{-L/2}^{L/2}\left(-x\frac{\dot{Y}}{\overline{Y}}+C_1(t)\right)dx=C_1(t) \tag{33}$$

and we conclude that $C_1(t)\equiv U(t)$ is a space-independent unsteady component of the flow velocity, related to the mean flow-rate generated by the pressure gradient $P_A>P_B$. Hence, we will use in the following the notation $U(t)$ instead of $C_1(t)$.

3. Linearized formulation

First note that, if the flow motion never reverses its direction (because of a large ratio P_A/P_B or of a small vibration amplitude), then we can replace $u(x,t)\,|u(x,t)|$ by $u(x,t)^2$, $\overline{K}_A\equiv K_A=K_{In}$ and $K_B\equiv K_B=K_{Out}$. Then, Eqs. (30) and (31) simplify considerably

$$\begin{aligned}F_f(t)=&\frac{L}{2}(P_A+P_B)-\frac{\rho L^3}{12}\frac{\ddot{Y}}{Y}+\frac{\rho L^3}{8}\left(\frac{1}{3}-\frac{K_A-K_B}{2}\right)\frac{\dot{Y}^2}{Y^2}\\&-\frac{\rho L}{2}\left(1+\frac{K_A-K_B}{2}\right)U(t)^2-\frac{\rho L^2}{2}\left(\frac{Lf}{3Y}+\frac{K_A+K_B}{2}\right)\frac{\dot{Y}}{Y}U(t)\end{aligned} \tag{34}$$

with

$$\begin{aligned}\dot{U}(t)=&\frac{1}{\rho L}(P_A-P_B)-\left(\frac{K_A+K_B}{2L}+\frac{f}{Y}\right)U(t)^2\\&-\frac{K_A-K_B}{2}\frac{\dot{Y}}{Y}U(t)-\frac{L}{4}\left(\frac{K_A+K_B}{2}+\frac{fL}{3Y}\right)\frac{\dot{Y}^2}{Y^2}\end{aligned} \tag{35}$$

We now look at the case of motions $Y(t)$ such that the fluctuating part $\tilde{Y}(t)$ is small when compared with the mean fluid gap $\overline{h}(x)=\overline{Y}$ under flow conditions. We then linearize Eq. (32), with Eqs. (34) and (35), about the mean amplitude, with

$$\begin{aligned}&Y(t)=\overline{Y}+\tilde{Y}(t),\qquad U(t)=\overline{U}+\tilde{U}(t)\\&F_f(t)=\overline{F}_f+\tilde{F}_f(t),\quad F_e(t)=\overline{F}_e+\tilde{F}_e(t)\end{aligned} \tag{36}$$

Then, inserting Eq. (36) into the dynamical equations, we obtain a pair of zero-order (static) equations, which describe the steady part of the flow, as well as to a couple of first-order (dynamic) equations describing the fluctuating flow, which are linearized, by dropping all higher-order terms:

(a) Zero-order equations

From Eq. (34) the average flow force per unit width reads

$$\overline{F}_f=L\left[\frac{P_A+P_B}{2}-\frac{1}{2}\rho\overline{U}^2\left(1+\frac{K_A-K_B}{2}\right)\right] \tag{37}$$

and the average axial flow velocity stemming from Eq. (35)

$$\overline{U}=\left[\frac{P_A-P_B}{\rho\left(\frac{K_A+K_B}{2}+\frac{L}{\overline{Y}}f\right)}\right]^{1/2} \tag{38}$$

Hence, from Eqs. (32) and (37)

$$K_s\left[\overline{Y}-H\right]=L_zL\left[\frac{P_A+P_B}{2}-\frac{1}{2}\rho\overline{U}^2\left(1+\frac{K_A-K_B}{2}\right)\right]+\overline{F}_e \tag{39}$$

from which we obtain the mean height of the fluid gap

$$\overline{Y}=H+\frac{1}{K_s}\left\{L_zL\left[\frac{P_A+P_B}{2}-\frac{1}{2}\rho\overline{U}^2\left(1+\frac{K_A-K_B}{2}\right)\right]+\overline{F}_e\right\} \tag{40}$$

(b) First-order equations

From Eq. (34) the linearized dynamical flow force per unit width reads

$$\begin{aligned}\tilde{F}_f(t)=&-\frac{\rho L^3}{12\overline{Y}}\ddot{\tilde{Y}}(t)-\overline{U}\frac{\rho L^2}{2\overline{Y}}\left(\frac{K_A+K_B}{2}+\frac{fL}{3\overline{Y}}\right)\dot{\tilde{Y}}(t)\\&-\overline{U}\rho L\left(1+\frac{K_A-K_B}{2}\right)\tilde{U}(t)\end{aligned} \tag{41}$$

and, from Eq. (35), we obtain the fluctuating flow velocity

$$\dot{\tilde{U}}(t)=-\overline{U}\frac{K_A-K_B}{2\overline{Y}}\dot{\tilde{Y}}(t)+\overline{U}^2\frac{f}{\overline{Y}^2}\tilde{Y}(t)-\overline{U}\left(\frac{K_A+K_B}{L}+2f\overline{Y}\right)\tilde{U}(t) \tag{42}$$

We then obtain the linearized dynamical equation, from Eqs. (32) and (41)

$$M_s\ddot{\tilde{Y}}+C_s\dot{\tilde{Y}}+K_s\tilde{Y}=L_z\tilde{F}_f(t)+\tilde{F}_e(t) \tag{43}$$

which is linearly coupled with (41), and (42).

Note that the fluctuating force $\tilde{F}_f(t)$ depends on the mean flow velocity $\overline{U}$ and on the average fluid gap $\overline{Y}$, which is a typical result for systems subjected to permanent flows. Therefore, unstable solutions become a distinct possibility. Under no-flow conditions, $\overline{U}=0$, solution (41) reverts to the classic added-mass term:

$$\tilde{F}_f(t)\Big|_{\overline{U}=0}=-\frac{\rho L^3}{12\overline{Y}}\ddot{\tilde{Y}}(t) \tag{44}$$

For the general case $\overline{U}>0$, Eqs. (41) and (42) are coupled, and both equations must be used simultaneously when computing the actual motions of the system. Formulation (42) can be seen as a first order differential equation in $\tilde{U}(t)$, which is forced by the plate motion $\tilde{Y}(t)$. In general this means there is a phase lag between $\tilde{Y}(t)$ and $\tilde{U}(t)$. Another way to look at these results is to transform Eqs. (41) and (42) for the case of pure oscillatory motions:

$$\tilde{F}_f(t)=\hat{F}_f e^{i\omega t},\quad \tilde{Y}(t)=\hat{Y}e^{i\omega t},\quad \tilde{U}(t)=\hat{U}e^{i\omega t} \tag{45}$$

where $\hat{F}_f$, $\hat{Y}$ and $\hat{U}$ are complex amplitudes. We then obtain

$$\hat{U}=\frac{\overline{U}^2\frac{f}{\overline{Y}^2}-\overline{U}\frac{K_A-K_B}{2\overline{Y}}i\omega}{\overline{U}\left(\frac{K_A+K_B}{L}+\frac{2f}{\overline{Y}}\right)+i\omega}\hat{Y} \tag{46}$$

leading to

$$\hat{F}_f=\left[\begin{array}{l}\dfrac{\rho L^3}{12\overline{Y}}\omega^2-\overline{U}\dfrac{\rho L^2}{2\overline{Y}}\left(\dfrac{K_A+K_B}{2}+\dfrac{fL}{3\overline{Y}}\right)i\omega-\\[2ex]-\overline{U}\rho L\left(1+\dfrac{K_A-K_B}{2}\right)\dfrac{\overline{U}^2\dfrac{f}{\overline{Y}^2}-\overline{U}\dfrac{K_A-K_B}{2\overline{Y}}i\omega}{\overline{U}\left(\dfrac{K_A+K_B}{L}+\dfrac{2f}{\overline{Y}}\right)+i\omega}\end{array}\right]\hat{Y} \tag{47}$$

This linearized solution is similar to the one produced by Porcher and DeLangre [10]. It is also compatible with the solution obtained by Inada and Hayama [7]. It is clear that, as a result of permanent flow and dissipative effects, both the velocity-coupling and the stiffness-coupling terms become frequency-dependent in Eq. (47). This physical result can create computational problems if one insists on having an explicit form, such as Eq. (47), for the dynamic flow force. We believe that keeping paired equations such as in (30),(31) or (41),(42) leads to much simpler computational work, either when seeking the time-domain nonlinear solutions or when computing the eigenvalues of the corresponding

linearized formulation. Indeed, by using this approach, frequency-dependent coupling coefficients never surface, so there is no need for iterative or other delicate numerical procedures. This significant point is further elaborated by Moreira et al. [13].

4. Numerical simulations

4.1. General procedure

Because we are dealing with a single-degree-of-freedom system, the flow-structure dynamical equation is simply

$$M_s\ddot{Y}+C_s\dot{Y}+K_s[Y-H]=L_zF_f(Y,\dot{Y},\ddot{Y},U(Y,\dot{Y}))+F_e(t) \tag{48}$$

where following Eq. (31) with the notation suggested by Eq. (33), the unsteady axial velocity is given by the first-order equation:

$$\dot{U}=\Phi(U,Y,\dot{Y}) \tag{49}$$

In state-space form, Eqs. (48) and (49) are equivalent to a system of three first-order equations:

$$\begin{aligned}&\dot{X}_1=X_2\\&\dot{X}_2=\frac{1}{M_s}\left\{-C_sX_2-K_s[X_1-H]+L_zF_f(X_1,X_2,\dot{X}_2,U(X_1,X_2))+F_e(t)\right\}\\&\dot{U}=\Phi(U,X_1,X_2)\end{aligned} \tag{50}$$

where $X_1=Y$ and $X_2=\dot{Y}$. One can notice that the inertial term $\dot{X}_2$ appears in both sides of the second Eq. (50), which must be modified as

$$\dot{X}_2=\frac{X_1}{M_sX_1+M_f}\{-C_sX_2-K_s[X_1-H]+G_f(X_1,X_2,U(X_1,X_2))+F_e(t)\} \tag{51}$$

For instance, for the simpler case with no permanent flow, Eqs. (50) and (51) become

$$\begin{aligned}&\dot{X}_1=X_2\\&\dot{X}_2=\frac{X_1}{M_sX_1+\dfrac{\rho L^3L_z}{12}}\left\{\begin{array}{l}-C_sX_2-K_s[X_1-H]\\+L_z\left[P_{ext}L+\dfrac{\rho L^3}{24}\dfrac{X_2^2}{X_1^2}-\dfrac{\rho L^4f}{32}\dfrac{X_2|X_2|}{X_1^3}-\dfrac{\rho L^3\overline{K}}{8}\dfrac{X_2|X_2|}{X_1^2}\right]\\+F_e(t)\end{array}\right\}\\&U=0,\quad\forall t\end{aligned} \tag{52}$$

The general case $U(t)\neq 0$ is obviously more involved, as follows from Eqs. (30) and (31).

4.2. Nonlinear analysis of a gravity-driven impacting plate

Our first example is closely related to the original industrial problem which motivated this study. An immersed rectangular plate with mass $M_s=36$ kg and axial length $L_x\equiv L=43$ mm (transverse width is $L_z=214$ mm) is dropped from a height $Y(0)=6$ mm. The plate is free to move along the vertical direction, when subjected to gravity, so that $K_s=0$. However, there is some damping $C_s=200$ N s/m in a plate-guiding fixture, as identified from an experimental rig at CEA (Saclay) connected with this problem (see [23]). The fluid is water, with volumic mass $\rho=1000$ kg/m^3 and kinematic viscosity $\nu=10^{-6}$ m^2/s.

Nonlinear time-domain computations were performed for three values of $\Delta P=P_A-P_B$, namely 0, 0.4 and 1 bar. The singular loss coefficients used in these computations were $K_A=K_B=1$. The friction coefficient f for the distributed pressure-drop was computed from formulation (16), using in each case an average value of the Reynolds number along the flow channel.

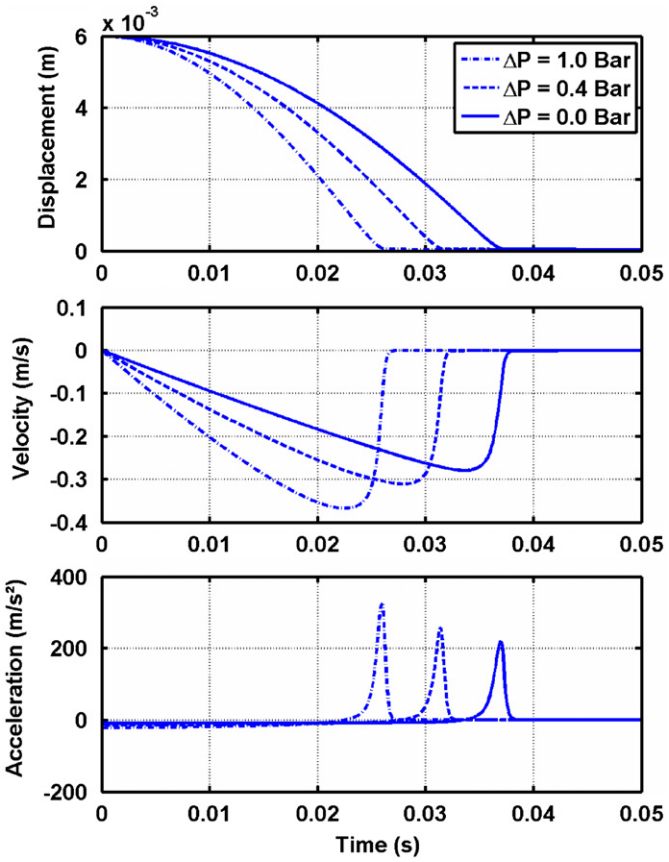

Fig. 3. Motion of the dropping mass as a function of the pressure difference ΔP.

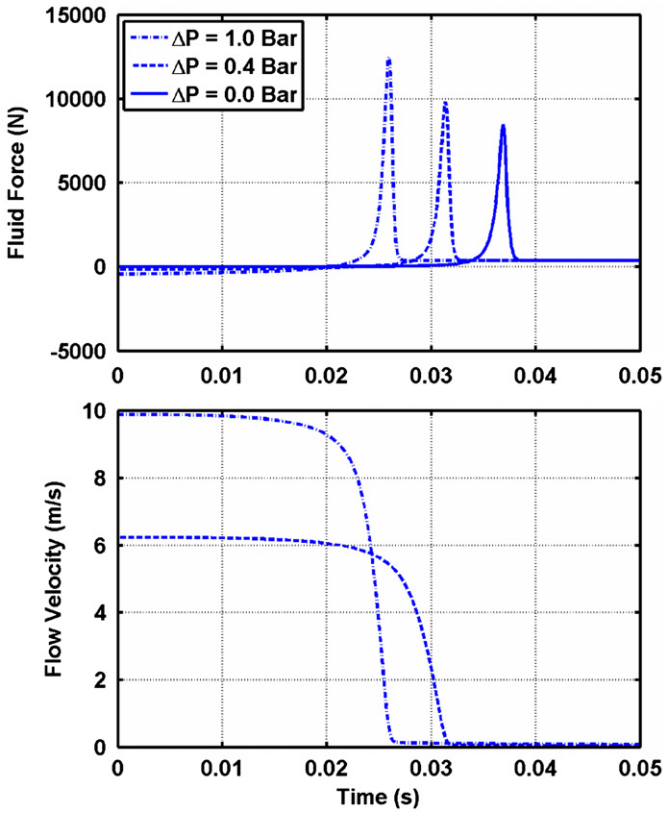

Fig. 4. Flow force on the dropping mass and axial flow velocity as a function of the pressure difference ΔP.

Fig. 3 shows how the axial flow, due to ΔP, affects the motion of the dropping plate. One can notice that, as the pressure gradient increases, the mass drops faster, until the flow becomes almost obstructed by the closing gap. This dynamic behavior can be related to a "sucking" Bernoulli effect of the axial flow. Accordingly, the dropping time is smaller and the motion velocity is higher when ΔP increases. Fig. 4 shows that the flow interaction force and the axial flow velocity also increase with ΔP, as might be expected.

4.3. Nonlinear analysis of a vibrating plate subjected to axial flow

We now turn to the case of a light elastically suspended plate with mass $M_s=0.05$ kg and axial length $L_x \equiv L=40$ mm (transverse width is $L_z=200$ mm). The stiffness and damping constants of the plate fixture are $K_s=2\times10^4$ N/m and $C_s=0.0628$ N s/m, respectively. These lead to modal frequency and damping values of $f_s=100$ Hz and $\zeta_s=0.1\%$. The working fluid is air, with volumic mass $\rho=1.2$ kg/m^3 and kinematic viscosity $\nu=1.5\times10^{-5}$ m^2/s. The parameter values in this example were selected aiming a light structure with "simple" values of the modal parameters f_s and ζ_s, which could become statically or dynamically unstable when subjected to an air flow of sufficient velocity.

In the computations presented in this section we used a friction coefficient $f=0.01$ for computing the distributed wall/flow stresses, as well as a loss coefficient at the inlet $K_A=0.5$ higher than the loss coefficient at the outlet $K_B=0.2$. Actually, in agreement with other investigators, we have found that the present model always leads to a stable system when a high value of the loss coefficient is imposed at the outlet (see, for instance, [10]). In practice, this means that a suitable outlet geometry with gradual transition and comparatively small losses would be necessary, in order for the system to display unstable motion regimes (see [25]). Nonlinear time-domain computations were performed for several values of $\Delta P=P_A-P_B$ and of the reference fluid gap H.

From the extensive time-domain computations performed, we selected a few cases for presentation here. In order to minimize the duration of the response transients in the results presented, we decided to start the dynamical computations after a pre-computation of the near-steady axial velocity. This was achieved by first "blocking" the plate at the reference value $Y=H$ and then calculating the resulting steady flow velocity $\overline{U}^{(Y=H)}$, from Eq. (38). Under these conditions, the structure is acted by a steady force $\overline{F}_f^{(Y=H)}$ per unit width given by Eq. (37), which is typically dominated by a Bernoulli effect of the flow, causing the moving plate to be "sucked" towards the base plate. The time-domain numerical simulations next shown are started using the initial conditions $Y(0)=H$, $\dot{Y}(0)=0$ and $U(0)=\overline{U}^{(Y=H)}$. Note that this pre-computation to obtain an estimate of the near-steady axial velocity is not an essential step of the procedure. Indeed, we could as well start our numerical simulations from a motionless fluid $U(0)=0$, which would then be accelerated by the pressure difference ΔP. The time-domain solution would obviously be different and with a longer transient response, but the underlying physics would be the same. On the other hand, because the moving plate is typically acted both sides by the average atmospheric pressure, the average value of P_A and P_B in solutions (30) or (34) is irrelevant. Therefore, in order to plot here fluid forces $F_f(t)$ which only represent the dynamical part of the solutions, we will choose always $P_A=P_B+\Delta P$ such that $P_A+P_B=0$.

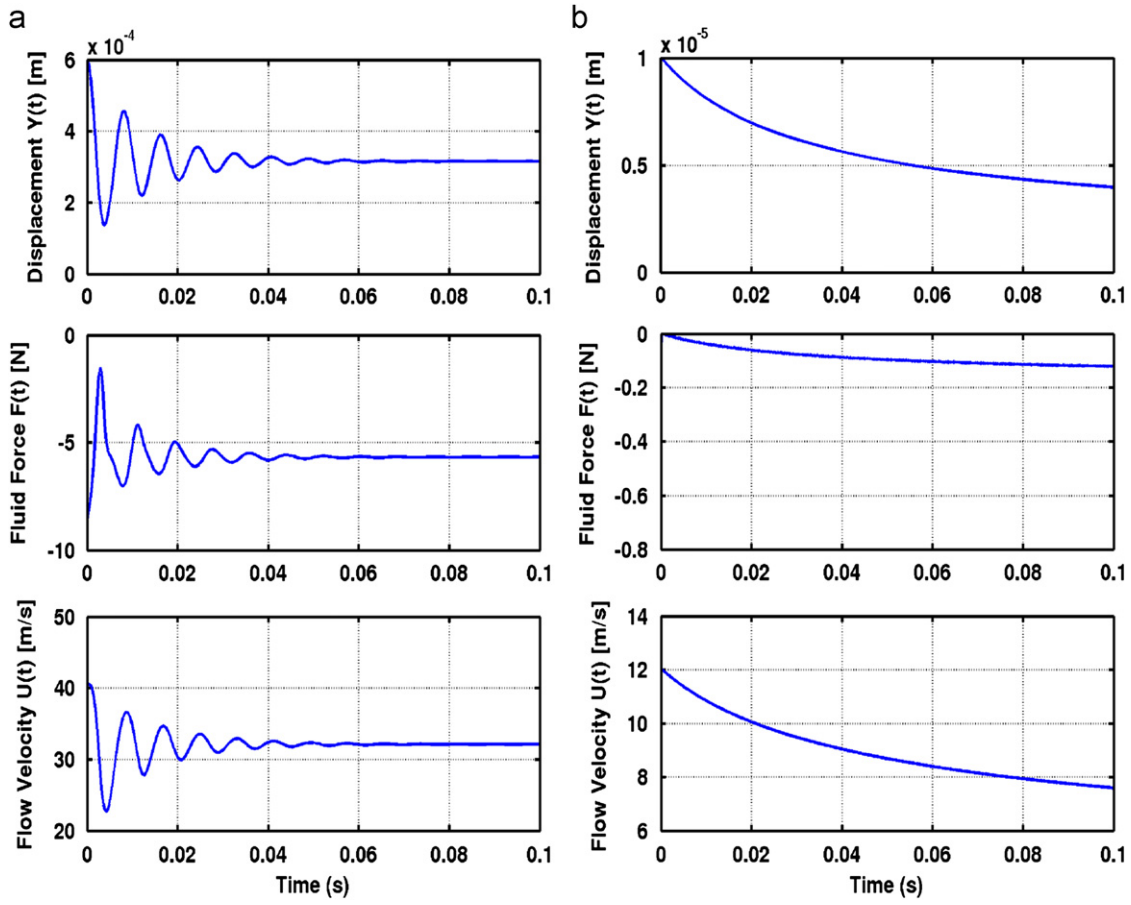

Fig. 5. Responses of a vibrating plate subjected to axial flow: (a) reference fluid gap $H=0.6$ mm and $\Delta P=0.02$ bar and (b) reference fluid gap $H=0.01$ mm and $\Delta P=0.07$ bar.

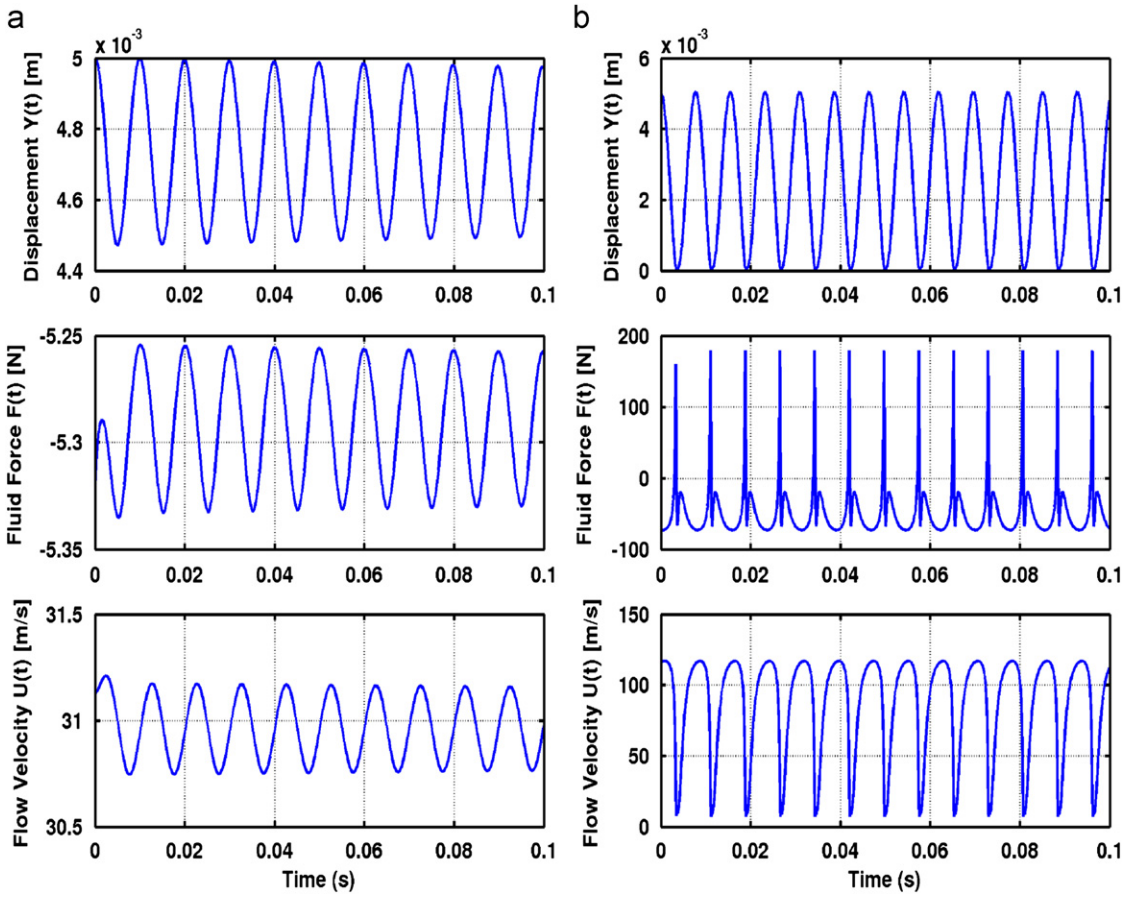

Fig. 6. Responses of a vibrating plate subjected to axial flow: (a) reference fluid gap $H=5$ mm and $\Delta P=0.005$ bar and (b) reference fluid gap $H=5$ mm and $\Delta P=0.07$ bar.

The first computational examples, shown in Fig. 5 pertain to a system configuration with small reference fluid gaps. In the left-side plots (a), we have $H=0.6$ mm under stagnant conditions and apply a pressure difference $\Delta P=0.02$ bar. The system motion is damped, tending to a final fluid gap of $\overline{Y}(t\to\infty)\simeq 0.32$ mm, with average flow velocity $\overline{U}(t\to\infty)\simeq 32\,m/s$ and a steady flow force $\overline{F}(t\to\infty)\simeq -5.5$ N (see Eqs. (37), (38) and (40)). As can be noticed from the plots, the corresponding initial values at $Y(0)=H$, computed from Eqs. (37) and (38) (with $\overline{Y}$ replaced by H), were $\overline{U}(0)=40.5\,m/s$ and $\overline{F}(0)\simeq -9.0$ N.

The computation results in the right side (b) of Fig. 5 were obtained by considering a smaller gap $H=0.01$ mm and imposing a larger pressure difference $\Delta P=0.07$ bar. Actually, for the specific parameters of this computation, the system is buckling, as was confirmed by time-domain computations using the linearized flow formulation (41) and (42). This point will be further discussed in the next section. Notice for the moment that, due to suction by the permanent flow, the fluid gap decreases asymptotically to about $\overline{Y}(t\to\infty)\simeq 0.002$ mm, with the average flow velocity tending to $\overline{U}(t\to\infty)\simeq 5.5\,m/s$ and the steady flow force to $\overline{F}(t\to\infty)\simeq -0.17$ N. The initial values at $Y(0)=H$ were $\overline{U}(0)=12.0\,m/s$ and $\overline{F}(0)\simeq -0.8$ N. In the plot, the transition from this value of the fluid force to almost zero is extremely fast, as a result of the zero stiffness of the flow/structure coupled system system.

The examples shown in Fig. 6 pertain to a configuration with a much larger reference gap, $H=5$ mm. In the left-side plots (a), a small pressure difference $\Delta P=0.005$ bar was imposed, resulting in a final fluid gap of $\overline{Y}(t\to\infty)\simeq 4.7$ mm, with average flow velocity $\overline{U}(t\to\infty)\simeq 30.9\,m/s$ and a steady flow force $\overline{F}(t\to\infty)\simeq -5.29$ N. The system response is almost harmonic and only slightly damped, therefore such configuration might well be computed using the linearized formulation (41) and (42) instead of the nonlinear model (30) and (31). In contrast to the preceding case, the results shown in the right-side plots obtained with $\Delta P=0.07$ bar clearly pertain to a linearly unstable system. Here, as will be shown in the next section, the linearized system becomes unstable by flutter. Then, limit cycles arise as a result of the nonlinear flow force terms, which limit the motion amplitude. Here, the flow force clearly behaves in a non-harmonic manner, with high-amplitude spikes whenever the gap nearly closes. Accordingly, the axial flow velocity is very unsteady, pulsating at the motion frequency.

4.4. Linearized analysis of a vibrating plate subjected to axial flow

The last example of the preceding section demonstrates the practical interest of the present nonlinear flow solution. Nevertheless, it also proves useful to get a global picture of the dynamical behavior and stability of the system, based on the linearized formulation provided by Eq. (43), with Eqs. (41) and (42). This is easily investigated by computing, for a given structure and flow, the eigenvalues of the following problem:

$$\left[M_s+\frac{\rho L^3 L_z}{12\overline{Y}}\right]\ddot{\tilde{Y}}+\left[C_s+\overline{U}\frac{\rho L^2 L_z}{2\overline{Y}}\left(\frac{K_A+K_B}{2}+\frac{fL}{3\overline{Y}}\right)\right]\dot{\tilde{Y}}+K_s\tilde{Y}$$
$$+\overline{U}\rho L L_z\left(1+\frac{K_A-K_B}{2}\right)\tilde{U}=0 \qquad (53)$$

or, defining the added mass $M_a = \rho L^3 L_z/(12\overline{Y})$

$$[M_s+M_a]\ddot{\tilde{Y}} + \left[C_s+\overline{U}M_a\frac{6}{L}\left(\frac{K_A+K_B}{2}+\frac{fL}{3\overline{Y}}\right)\right]\dot{\tilde{Y}} + K_s\tilde{Y} + \overline{U}M_a\frac{12\overline{Y}}{L^2}\left(1+\frac{K_A-K_B}{2}\right)\tilde{U} = 0 \tag{54}$$

and

$$\dot{\tilde{U}} + \overline{U}\frac{K_A-K_B}{2\overline{Y}}\dot{\tilde{Y}} - \overline{U}^2\frac{f}{\overline{Y}^2}\tilde{Y} + \overline{U}\left(\frac{K_A+K_B}{L}+2f\overline{Y}\right)\tilde{U} = 0 \tag{55}$$

where the mean values of the flow velocity $\overline{U}$ and fluid gap $\overline{Y}$ are given by Eqs. (38) and (40), respectively. Then, following the usual procedure for state-space formulation:

$$\begin{Bmatrix}\dot{\tilde{X}}_1\\ \dot{\tilde{X}}_2\\ \dot{\tilde{U}}\end{Bmatrix} = \begin{bmatrix} 0 & 1 & 0\\ -\frac{K_s}{M_s+M_a} & -\frac{C_s+\overline{U}M_a\frac{6}{L}\left(\frac{K_A+K_B}{2}+\frac{fL}{3\overline{Y}}\right)}{M_s+M_a} & -\frac{\overline{U}M_a\frac{12\overline{Y}}{L^2}\left(1+\frac{K_A-K_B}{2}\right)}{M_s+M_a}\\ \overline{U}^2\frac{f}{\overline{Y}^2} & -\overline{U}\frac{K_A-K_B}{2\overline{Y}} & -\overline{U}\left(\frac{K_A+K_B}{L}+\frac{2f}{\overline{Y}}\right)\end{bmatrix}\begin{Bmatrix}\tilde{X}_1\\ \tilde{X}_2\\ \tilde{U}\end{Bmatrix} \tag{56}$$

where $\tilde{X}_1 = \tilde{Y}$ and $\tilde{X}_2 = \dot{\tilde{Y}}$. Hence, the dynamical behavior and stability of the linearized system is described in terms of the eigenvalues λ_n and eigenvectors $\{X_n\}$ of

$$([\mathbf{A}]-\lambda[\mathbf{I}])\begin{Bmatrix}\hat{X}_1\\ \hat{X}_2\\ \hat{U}\end{Bmatrix} = \{\mathbf{0}\} \tag{57}$$

Eq. (56) can be easily formulated in dimensionless terms, by introducing the circular frequency and damping ratio of the system in still water:

$$\omega_0^2 = \frac{K_s}{M_s+M_a}, \quad \zeta_0 = \frac{C_s}{2(M_s+M_a)\omega_0} = \frac{C_s}{2\sqrt{K_s(M_s+M_a)}} \tag{58}$$

as well as the following reduced quantities, which arise naturally from the previous results:

$$\eta = \frac{M_a}{M_s+M_a}, \quad \varepsilon = \frac{\overline{Y}}{L}, \quad \tau = \omega_0 t, \quad \overline{\mathcal{U}} = \frac{\overline{U}}{\omega_0\overline{Y}}$$

$$\tilde{\mathcal{X}}_1 \equiv \tilde{\mathcal{Y}} = \frac{\tilde{Y}}{\overline{Y}} \Rightarrow \tilde{\mathcal{X}}_2 \equiv \dot{\tilde{\mathcal{Y}}} = \frac{\dot{\tilde{Y}}}{\omega_0\overline{Y}} \Rightarrow \ddot{\tilde{\mathcal{Y}}} = \frac{\ddot{\tilde{Y}}}{\omega_0^2\overline{Y}}, \quad \tilde{\mathcal{U}} = \frac{\tilde{U}}{\omega_0\overline{Y}} \Rightarrow \dot{\tilde{\mathcal{U}}} = \frac{\dot{\tilde{U}}}{\omega_0^2\overline{Y}} \tag{59}$$

and we obtain

$$\begin{Bmatrix}\dot{\tilde{\mathcal{X}}}_1\\ \dot{\tilde{\mathcal{X}}}_2\\ \dot{\tilde{\mathcal{U}}}\end{Bmatrix} = \begin{bmatrix} 0 & 1 & 0\\ -1 & -2\zeta_0-6\overline{\mathcal{U}}\eta\varepsilon\left(\frac{K_A+K_B}{2}+\frac{f}{3\varepsilon}\right) & -12\overline{\mathcal{U}}\eta\varepsilon^2\left(1+\frac{K_A-K_B}{2}\right)\\ \overline{\mathcal{U}}^2 f & -\overline{\mathcal{U}}\frac{K_A-K_B}{2} & -\overline{\mathcal{U}}(\varepsilon(K_A+K_B)+2f)\end{bmatrix}\begin{Bmatrix}\tilde{\mathcal{X}}_1\\ \tilde{\mathcal{X}}_2\\ \tilde{\mathcal{U}}\end{Bmatrix} \tag{60}$$

Eq. (60) highlights the significance of the scaling factors (59), for vibratory problems under axial flow, in particular the mass ratio η, the reduced gap ε and reduced axial flow velocity $\overline{\mathcal{U}}$. Even so, the resulting system is still quite complex and it is hard to extract any general conclusions concerning the effects of the various friction coefficients on the dynamics of the flow-coupled system. These will be highlighted in the following through a number of illustrative computations.

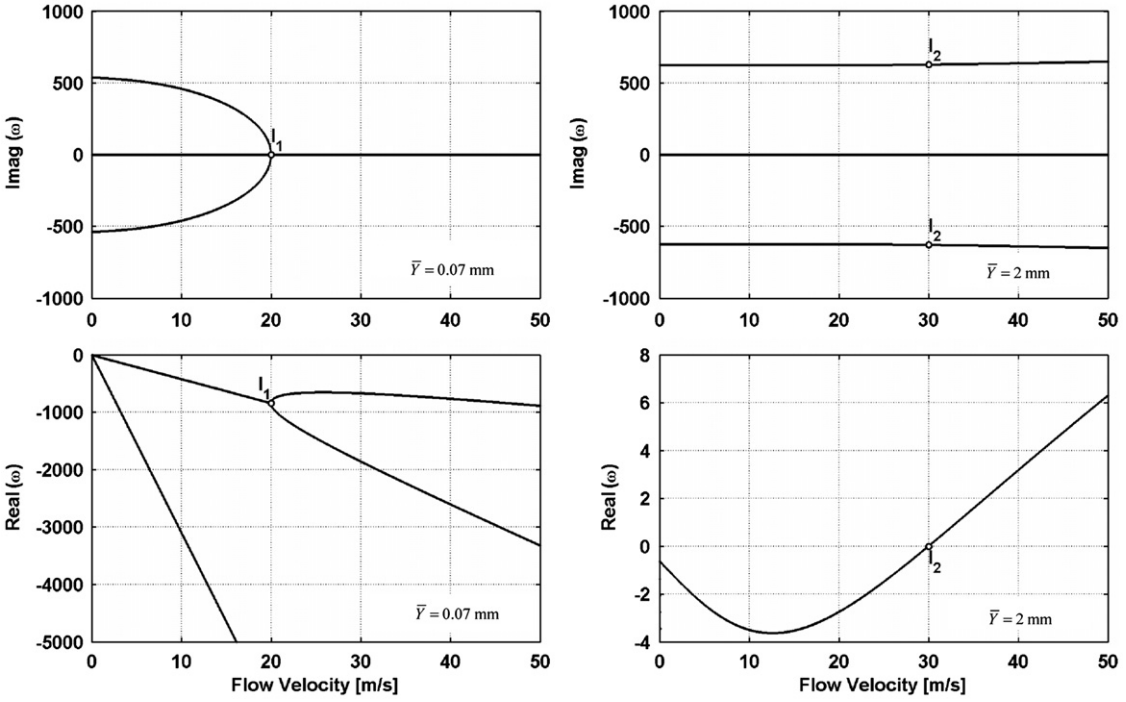

Fig. 7. Eigenvalues for a vibrating plate subjected to axial flow, for two reference fluid gaps $\overline{Y} = 0.07$ and 2 mm, with $K_A = 0.5$, $K_B = 0.2$ and $f = 0.01$.

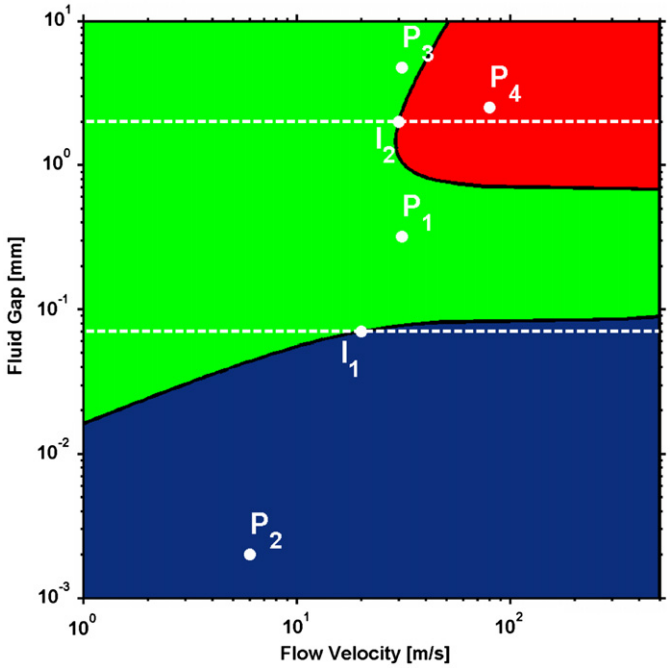

Fig. 8. Stability map for a vibrating plate subjected to axial flow, as a function of $\overline{U}$ and $\overline{Y}$, for $K_A=0.5$, $K_B=0.2$ and $f=0.01$.

Plots of the real and imaginary parts of the three eigenvalues $\lambda_n(\overline{U})=\sigma_n(\overline{U})\pm i\omega_n(\overline{U})$ of Eq. (57), as a function of the steady flow velocity $\overline{U}$, are shown in Fig. 7, for two values of the mean fluid gap, $\overline{Y}=0.07$ and 2 mm. They were computed using values $K_A=0.5$, $K_B=0.2$ and $f=0.01$ for the loss coefficients. In the left-side plots, pertaining to configuration $\overline{Y}=0.07$ mm, increasing the flow velocity $\overline{U}$ decreases the damped modal frequency $\pm\omega_n$, until the stiffness of the system becomes nil at about $\overline{U}\simeq 20\,m/s$. At this velocity (point I_1 in the plots), *buckling* of the system arises. In the right-side plots, corresponding to configuration $\overline{Y}=2$ mm, increasing the flow velocity barely changes the modal frequency. However, large changes are displayed by the real part σ_n of the eigenvalues, which first decrease (e.g., damping $\zeta_n=-\sigma_n/|\lambda_n|$ increases) until flow velocity is about $\overline{U}\simeq 12\,m/s$, and then start increasing (damping ζ_n decreases). When the flow velocity is about $\overline{U}\simeq 30\,m/s$ (point I_2 in the plots), σ_n becomes positive ($\zeta_n<0$) and the system is unstable by *flutter*.

Fig. 8 displays a more complete scenario, by plotting the stability map for the loss coefficients $K_A=0.5$, $K_B=0.2$ and $f=0.01$, as a function of the mean flow velocity $\overline{U}$ and average operation gap $\overline{Y}$. The three dynamical regions previously described are shown through the following color code: *green* for a stable system, *blue* for buckling and *red* for flutter. The lines highlighted in the map pertain to the eigen-solutions presented in Fig. 7, respectively, for $\overline{Y}=0.07$ mm (with buckling at point I_1) and $\overline{Y}=2$ mm (with flutter at point I_2). Also, four points P_1–P_4 highlighted in the map represent the asymptotic values of $\overline{Y}$ and

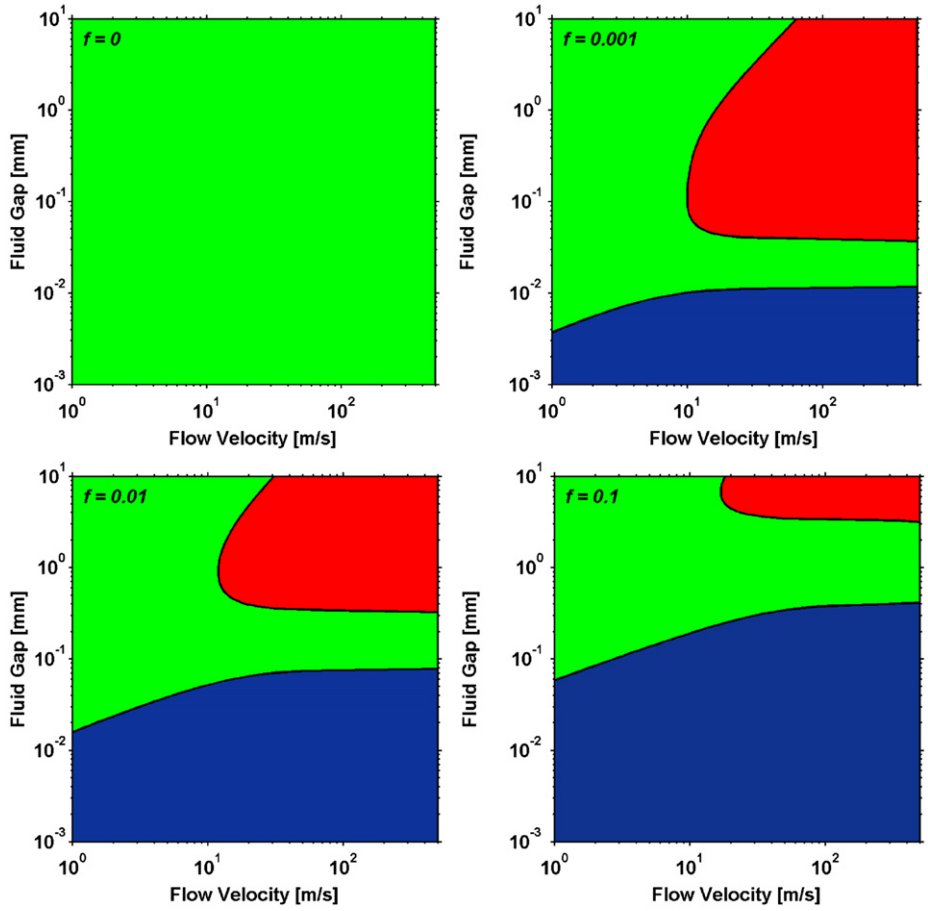

Fig. 9. Stability maps for a vibrating plate subjected to axial flow, as a function of $\overline{U}$ and $\overline{Y}$, when $K_A=0$ and $K_B=0$, for $f=0$, 0.001, 0.01 and 0.1.

$\overline{U}$, as $t\to\infty$, for the time-domain computations shown in Figs. 5 and 6. Notice that, for the configuration P_1 shown in Fig. 5(a), the system is indeed stable. The same applies to the configuration P_3 shown in Fig. 6(a). On the other hand, as claimed before, configuration P_2 pertaining to the computation in Fig. 5(b) lays in the buckling region of the map. Finally, in agreement with the results of Fig. 6(b), configuration P_4 is linearly unstable by flutter.

Because stability maps such as the ones in Fig. 8 encapsulate much interesting information, Figs. 9–11 display several maps of the system as a function of $\overline{U}$ and $\overline{Y}$, to illustrate distinct conceptual scenarios depending on the values of K_A, K_B and f. For each stability map supplied we decided to postulate constant values for the friction coefficients, so that the effects of changing other parameters may be easily grasped. But obviously, in actual computations of practical interest, one cannot change the fluid gap and/or velocity while keeping the same friction coefficient. As discussed earlier, these coefficients must be adjusted accounting for the representative Reynolds numbers which stem from these parameters.

Fig. 9 shows the effect on the system stability of the distributed loss coefficient, in the range $0\le f\le 0.1$, when postulating no singular losses at the inlet and outlet, $K_A=K_B=0$. The system is always stable when $f=0$, however, even a small value of the friction coefficient will lead to divergence and flutter regions. As f increases, so does the extent of the divergence domain, while the size of the flutter domain decreases. Basically, the same conclusion can be drawn from Fig. 10, where we used $K_A=1$ and $K_B=0$, although the dynamical behavior when $f=0$ is now quite different from the previous case with no dissipative effects. Actually, when $K_A>K_B$, the three different regions in the stability map always arise, irrespectively of the value of the friction coefficient. Fig. 11, computed using $K_A=0$ and $K_B=1$, shows that when $K_A<K_B$ the system never displays the flutter instability.

5. Conclusions

We developed in this paper a theoretical model for the linear and nonlinear motions of parallel plates subjected to axial flows. The theory presented should be adequate for small and moderate fluid gaps. Flow was modeled using simplifying assumptions connected with the so-called bulk-flow approach, which preserves the inertial character of the flow, is well suited for turbulent flows and accounts for all spatial aspects in the Navier–Stokes equations using a single space coordinate. Both distributed and singular dissipative effects have been addressed, using empirical pressure-loss terms.

The formulation was illustrated with two examples, namely a gravity-driven impacting plate and a vibrating system. All test cases highlight the significance of the axial flow, even for a rigid impacting system. Solutions for vibrating systems clearly depend on both the mean axial flow velocity, the inlet and outlet boundary conditions, as well as on the average fluid gap. This was shown by computing an extensive set of stability charts and by performing nonlinear time-domain numerical simulations for both stable and unstable configurations. In agreement with

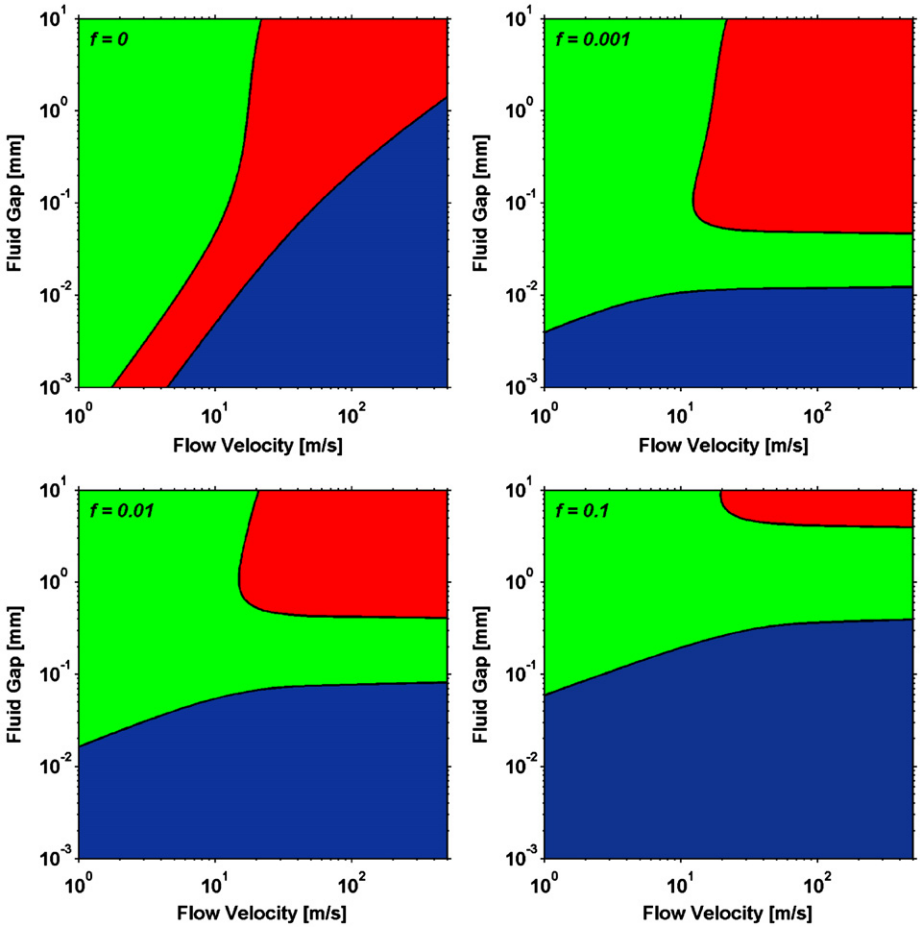

Fig. 10. Stability maps for a vibrating plate subjected to axial flow, as a function of $\overline{U}$ and $\overline{Y}$, when $K_A=1$ and $K_B=0$, for $f=0$, 0.001, 0.01 and 0.1.

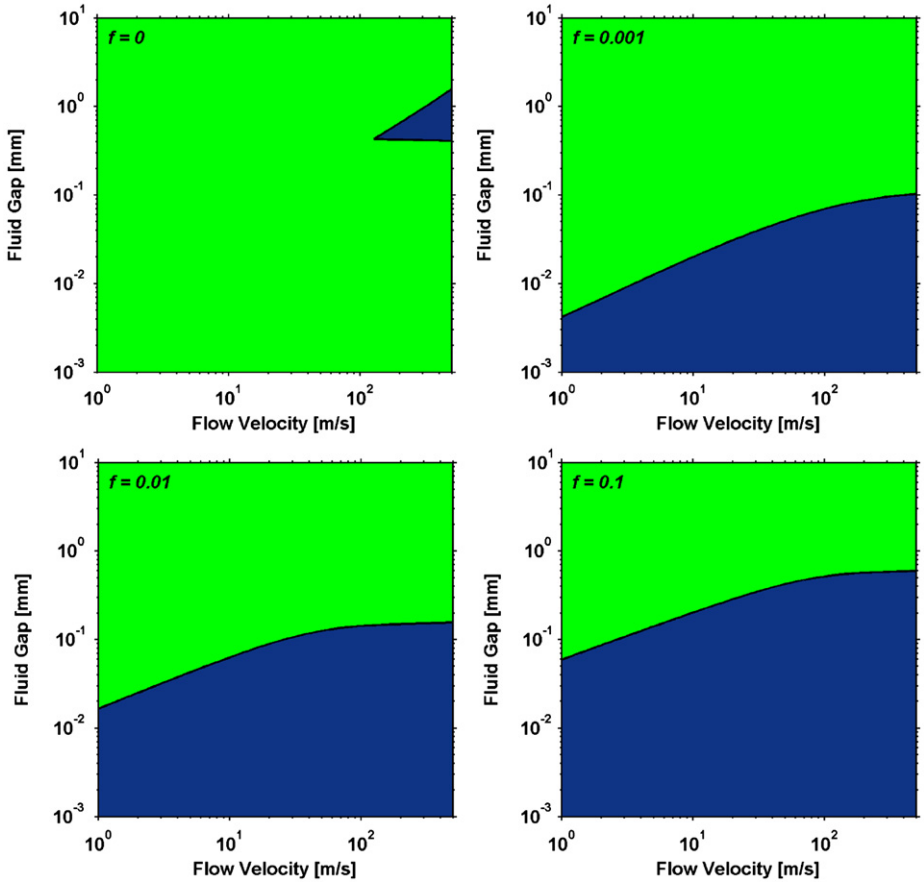

Fig. 11. Stability maps for a vibrating plate subjected to axial flow, as a function of $\overline{U}$ and $\overline{Y}$, when $K_A=0$ and $K_B=1$, for $f=0$, 0.001, 0.01 and 0.1.

previous studies (see [6,7,10,14,15]) the parametric analysis from the present model shows that increasing K_A has a destabilizing effect for the system, while increasing K_B has a stabilizing effect. On the other hand, increasing f is mostly destabilizing, depending on H.

Although this is a theoretical paper, which does not intend to address the important step of experimental validation, we have already performed extensive tests to validate the theoretical predictions for the symmetrical case $P_A=P_B$, with an overall satisfactory agreement (see [26]). The corresponding validation experiments under the axial flows generated when $P_A \neq P_B$ have yet to be performed.

This work was motivated by industry-related problems. Actually, in two related papers, Moreira and Antunes [28,29] show how the present model can be used effectively to predict the flow-structure dynamics of immersed spent nuclear fuel racks. These are stored in pools, often using a regular chessboard-type layout, with the neighboring racks separated by fluid channels such that $H/L \ll 1$. The rack dynamics under seismic excitation are conveniently addressed using, for each channel, the modeling approach developed in this paper. The closure of the formulation for the dynamical pressure and flow velocity fields is then obtained from the mass and pressure compatibility conditions at each corner, where four channels converge (see [28,29]). In a very different scientific field, the last example in this paper might well represent a typical response of the blown reed-valve embouchure of a musical instrument, when uncoupled from the acoustical field of the instrument pipe. The present model may well constitute an improvement over the usual approach based on a straight application of the quasi-static Bernoulli equation (see [30–32] for details).

References

[1] Esmonde H, Fitzpatrick J, Rice H, Axisa F. Analysis of nonlinear squeeze-film dynamics: I—physical theory and modeling. In: ASME pressure vessel and piping conference, Nashville, June 1990, USA.
[2] Esmonde H, Axisa F, Fitzpatrick J, Rice H. Analysis of nonlinear squeeze-film dynamics: II—experimental measurement and model verification. In: ASME pressure vessel and piping conference, June 1990, Nashville, USA.
[3] Fritz R. The effects of an annular fluid on the vibrations of a long rotor: Part 1—theory. ASME Journal of Basic Engineering 1970;92:923–9.
[4] Hobson DE. Fluid-elastic instabilities caused by flow in an annulus. In: Proceedings of the 3rd international conference on vibration in nuclear plant, Keswick, UK. BNES, London; p. 440–63.
[5] Mulcahy TM. Fluid forces on rods vibrating in a finite length annular region. ASME Journal of Applied Mechanics 1980;47:234–40.
[6] Mulcahy TM. One-dimensional leakage-flow vibration instabilities. Journal of Fluids and Structures 1988;2:383–403.
[7] Inada F, Hayama S. A study of leakage-flow-induced vibrations: Part 1—fluid dynamic forces and moments acting on the walls of a narrow tapered passage. Journal of Fluids and Structures 1990;4:395–412.
[8] Inada F, Hayama S. A study of leakage-flow-induced vibrations: Part 2—stability analysis and experiments for two-degree-of-freedom systems combining translational and rotational motions. Journal of Fluids and Structures 1990;4:413–28.
[9] Perotin L, Granger S. A linearized unsteady model for computing dynamics of cylindrical structures subjected to non-uniform annular flows at high Reynolds numbers. Journal of Fluids and Structures 1997;11:183–205.
[10] Porcher G, DeLangre E. A friction-based model for fluidelastic forces induced by axial flow. In: Proceedings of the 4th international symposium on fluid–structure interaction, November 1997, Dallas, USA.
[11] Inada F, Hayama S. Mechanism of leakage flow-induced vibrations—single-degree-of-freedom and continuous systems. In: Proceedings of the 7th international conference on flow-induced vibration (FIV2000), June 2000, Lucerne, Switzerland.
[12] Kaneko S, Tanaka S, Watanabe T. Leakage flow induced flutter of highly flexible structures. In: Proceedings of the 7th international conference on Flow-Induced Vibration (FIV2000), June 2000, Lucerne, Switzerland.

[13] Moreira M, Antunes J, Pina, H. An improved linear model for rotors subjected to dissipative annular flows. In: Proceedings of the 7th international conference on Flow-Induced Vibration (FIV2000), June 2000, Lucerne, Switzerland.
[14] Païdoussis MP. Fluid–structure interactions: slender structures and axial flow, vol. 1. San Diego, USA: Academic Press; 1998.
[15] Kaneko S, Nakamura T, Inada F, Kato M. Flow induced vibrations: classifications and lessons from practical experiences. Amsterdam, The Netherlands: Elsevier; 2008.
[16] Axisa F, Antunes J. Flexural vibrations of rotors immersed in dense fluids: Part 1—theory. Journal of Fluids and Structures 1992;6:3–21.
[17] Grunenwald T. Comportement Vibratoire d'Arbres de Machines Tournantes dans un Espace Annulaire de Fluide de Confinement Modéré. Doctoral Thesis, Paris University, September 1994.
[18] Antunes J, Axisa F, Grunenwald T. Dynamics of rotors immersed in eccentric annular flows: Part 1—theory. Journal of Fluids and Structures 1996;10:893–918.
[19] Antunes J, Mendes J, Moreira M, Grunenwald T. A theoretical model for nonlinear planar motions of rotors under fluid confinement. Journal of Fluids and Structures 1999;13:3–21.
[20] Moreira M, Antunes J, Pina H. A theoretical model for nonlinear orbital motions of rotors under fluid confinement. Journal of Fluids and Structures 2000;14:635–68.
[21] Hirs G. A bulk-flow theory for turbulence in lubricant films. ASME Journal of Lubrication Technology 1973;95:137–46.
[22] Childs D. Turbomachinery rotordynamics: phenomena. modeling and analysis. New York, USA: John Wiley & Sons; 1993.
[23] Piteau P, Antunes J, Borsoi L. Experimental validation of a nonlinear bulk-flow squeeze-film theoretical model. In: Proceedings of the 7th EUROMECH Solids Mechanics Conference (ESMC2009), September 2009, Lisbon, Portugal.
[24] Idel'Cik I. Memento des Pertes de Charge. Paris, France: Eyrolles [Also published in 1994 as Handbook of Hydraulic Resistance. Boca Raton, USA: CRC Press].
[25] Blevins R. Fluid dynamics. New York, USA: Van Nostrand Reinhold Company; 1984.
[26] Piteau P, Antunes J. Experiments on the nonlinear dynamics of parallel plates subjected to squeeze-film forces. In: Proceedings of the ASME 2010 10th biennial conference on Engineering Systems Design and Analysis (ESDA2010), July 2010, Istanbul, Turkey.
[27] Heal K, Hansen M, Rickard K. Maple V learning guide. New York, USA: Springer-Verlag; 1996.
[28] Moreira M, Antunes J. A simplified linearized model for the flow-coupled vibrations of spent nuclear fuel racks. Journal of Fluids and Structures 2002;16:971–87.
[29] Moreira M, Antunes J. Fluid-coupled vibrations of immersed spent nuclear racks: a nonlinear model accounting for squeeze-film and dissipative phenomena. In: ASME 2004 International Mechanical Engineering Congress and Exposition (IMECE2004), November 13–19, 2004, Anaheim, CA, USA, Paper no. IMECE2004-62353, p. 651–62.
[30] Hirschberg A, Kergomard J, Weinreich G. Mechanics of musical instruments. Vienna, Austria: Springer-Verlag; 1995.
[31] Fletcher N, Rossing T. The physics of musical instruments. New York, USA: Springer-Verlag; 1998.
[32] Chaigne A, Kergomard J. Acoustique des Instruments de Musique. Paris, France: Belin; 2008.